NN-RESDMD: LEARNING KOOPMAN REPRESENTATIONS FOR COMPLEX DYNAMICS WITH SPECTRAL RESIDUALS

Anonymous authors
Paper under double-blind review

ABSTRACT

Analyzing long-term behaviors in high-dimensional nonlinear dynamical systems remains a significant challenge. The Koopman operator framework has emerged as a powerful tool to address this issue by providing a globally linear perspective on nonlinear dynamics. However, existing methods for approximating the Koopman operator and its spectral components, particularly in large-scale systems, often lack robust theoretical guarantees. Residual Dynamic Mode Decomposition (ResDMD) introduces a spectral residual measure to assess the convergence of the estimated Koopman spectrum, which helps filter out spurious spectral components. Nevertheless, it depends on pre-computed spectra, thereby inheriting their inaccuracies. To overcome its limitations, we introduce the Neural Network-ResDMD (NN-ResDMD), a method that directly estimates Koopman spectral components by minimizing the spectral residual. By leveraging neural networks, NN-ResDMD automatically identifies the optimal basis functions of the Koopman invariant subspace, eliminating the need for manual selection and improving the reliability of the analysis. Experiments on physical and biological systems demonstrate that NN-ResDMD significantly improves both accuracy and scalability, making it an effective tool for analyzing complex dynamical systems.

1 INTRODUCTION

In the study of complex dynamical systems, a critical challenge lies in accurately extracting and analyzing long-term behavior in high-dimensional nonlinear systems. Various data-driven methods (Brunton & Kutz, 2019; Schetzen, 2006; Wiggins, 2003; Slotine & Li, 1991; Lan & Mezić, 2013; Mezić, 2005) have been developed to address this challenge, with the Koopman operator (Koopman, 1931; Koopman & Neumann, 1932) framework emerging as a powerful tool due to its ability to globally linearize nonlinear systems. Unlike local linearization methods (Hartman, 1960; Grobman, 1959), which approximate dynamics near fixed points, the Koopman operator transforms the entire system into a linear form within an infinite-dimensional space, which allows the use of spectral analysis techniques to study complex dynamics.

Despite its promise, practical computational challenges arise from the infinite-dimensional nature of the Koopman operator. Numerical methods such as Extended Dynamic Mode Decomposition (EDMD) (Williams et al., 2015) have been developed to approximate the Koopman operator using a finite set of observables, making it possible to extract dynamic modes from data. However, EDMD lacks theoretical guarantees of convergence and may fail to capture the full Koopman spectrum accurately, particularly in large-scale, complex systems.

To address these limitations, the Residual Dynamic Mode Decomposition (ResDMD) method (Colbrook & Townsend, 2024) was introduced, which offers convergence guarantees by using a spectral residual measure that quantifies the extent to which the estimated Koopman spectrum converges to the true spectrum of the system. By assessing the convergence, ResDMD can eliminate spurious spectral components—those that do not correspond to the true dynamics of the system—thereby enhancing the reliability and robustness of the spectral estimation. However, ResDMD primarily serves as a filtering tool for precomputed spectra rather than providing a direct and more accurate

approximation of Koopman spectra. Consequently, it lacks the capacity to independently refine the spectral estimation.

In this paper, we propose Neural Network-ResDMD (NN-ResDMD), which overcomes this limitation by providing a method to directly compute Koopman eigenpairs by minimizing the spectral residual. Additionally, NN-ResDMD employs neural networks to automatically select basis functions, eliminating the need for manual intervention, a common challenge in EDMD-based methods. Through experiments on both toy models and real-world high-dimensional systems, we demonstrate that NN-ResDMD significantly improves accuracy and scalability, making it a practical and effective tool for analyzing complex dynamical systems.

2 Preliminary on Koopman operator

Consider a discrete-time dynamical system (Ω, μ) governed by a map $F : \Omega \to \Omega$, where $\Omega \subseteq \mathbb{R}^d$ is the state space, and μ is a probability measure. The evolution of the system is described by:

$$x_{k+1} = F(x_k), \quad k \in \mathbb{Z}^+.$$

The Koopman operator $\mathcal{K}$ acts on observables $g \in L^2(\Omega, \mu)$ as:

$$\mathcal{K}g = g \circ F.$$

Although F is nonlinear, the Koopman operator $\mathcal{K}$ is linear, enabling spectral analysis of the system in the infinite-dimension function space.

A key aspect of modern Koopman operator theory is Koopman Mode Decomposition (KMD) (Mezić, 2005), which represents system dynamics through its spectral components, i.e. the eigenvalues, Koopman modes, and eigenfunctions. The discrete spectrum is particularly important for insights into long-term behavior, such as periodicity and stability. Our analysis emphasizes these spectral components derived from KMD. Specifically, we seek eigenpairs (λ_i, ϕ_i), where λ_i are eigenvalues and ϕ_i are the corresponding Koopman eigenfunctions.

One of the most prominent numerical methods to approximate the Koopman operator and its spectral components is the Extended Dynamic Mode Decomposition (EDMD) method, introduced by Williams et al. (2015). In EDMD, a set of observables (dictionary or basis functions) $\mathbf{\Psi} = [\psi_1, \ldots, \psi_{N_K}]$ is selected, and the span of these observables defines the subspace $V_{N_K} := \text{span}\{\psi_i\}_{i=1}^{N_K}$. Snapshots of the system's state are then collected, and the method constructs a finite-dimensional approximation of the Koopman operator by solving a least-squares problem that relates the snapshots of observables. This enables the computation of eigenvalues, eigenfunctions, and Koopman modes. Note that while common choices of dictionary functions are polynomials, Fourier basis, RBF functions, etc., the optimal choice of basis functions is usually unknown a priori and depends heavily on the specific dynamical system.

Given independent and identically distributed data snapshots $\{(x_i, y_i)\}_{i=1}^m$ with $y_i = F(x_i)$, two matrices Ψ_X and Ψ_Y are formed by evaluating the dictionary on the data snapshots:

$$\Psi_X = \begin{bmatrix} \psi_1(x_1) & \ldots & \psi_{N_K}(x_1) \\ \vdots & \ddots & \vdots \\ \psi_1(x_m) & \ldots & \psi_{N_K}(x_m) \end{bmatrix}, \quad \Psi_Y = \begin{bmatrix} \psi_1(y_1) & \ldots & \psi_{N_K}(y_1) \\ \vdots & \ddots & \vdots \\ \psi_1(y_m) & \ldots & \psi_{N_K}(y_m) \end{bmatrix}.$$

EDMD computes the Koopman matrix approximation as $K = \Psi_X^\dagger \Psi_Y$, where $\Psi_X^\dagger$ is the pseudo-inverse of Ψ_X. The eigenvalues of K provide approximations of the Koopman operator's spectrum, and the Koopman eigenfunctions ϕ_i are approximated as $\phi_i = \mathbf{\Psi}\mathbf{v}_i$, where $\mathbf{v}_i \in \mathbb{C}^{N_K}$ is the i-th eigenvector of K.

3 Koopman Operator Learning

While EDMD effectively approximates the Koopman operator, it still suffers from issues like spectral pollution. As the dictionary size increases, spurious eigenvalues can accumulate, leading to an inaccurate or over-saturated spectrum that misrepresents the system's true dynamics. This makes

it difficult to distinguish between meaningful dynamic modes and noise, ultimately reducing the accuracy of the analysis. To address these limitations, Residual Dynamic Mode Decomposition (ResDMD) (Colbrook & Townsend, 2024) filters out spurious eigenvalues by assessing their spectral residuals. However, ResDMD relies on precomputed eigenpairs, inheriting inaccuracies from methods like EDMD without directly improving the initial spectral estimation.

In contrast, we introduce the Neural Network-ResDMD (NN-ResDMD), a new method that provides a theoretically convergent way to approximate the Koopman operator and its spectral components by minimizing a ResDMD-specific loss function. Additionally, NN-ResDMD optimizes the dictionary functions for the Koopman invariant subspace using a Feedforward Neural Network (FNN), which eliminates the need for manual design of basis functions.

3.1 ResDMD Review

Now, suppose we have obtained an eigenpair (λ, ϕ) of $\mathcal{K}$ from EDMD or other methods (Colbrook, 2023b; Baddoo et al., 2021; Alford-Lago et al., 2022a; Schmid, 2010; Tu et al., 2014; Li et al., 2017; Takeishi et al., 2017a; Lusch et al., 2017; Takeishi et al., 2017b; Yeung et al., 2019a; Otto & Rowley, 2019a; Azencot et al., 2020b; Wu & Noé, 2020; Iwata & Kawahara, 2020) where $\lambda \in \mathbb{C}$ and the eigenfunction ϕ is expanded in terms of dictionary functions, i.e., $\phi = \mathbf{\Psi}\mathbf{v} = \sum_{i=1}^{N_K} \psi_i v_i \in V_{N_K}$ for some $\mathbf{v} \in \mathbb{C}^{N_K}$, where v_i represents weights of the span. Without loss of generality, we consider ϕ has been normalized, i.e., $\|\phi\|_2 = 1$. The accuracy of this eigenpair approximation in the ResDMD framework can be measured by computing its *squared relative residual* using the dictionary in the following way:

$$
\begin{aligned}
\mathit{res}(\lambda, \phi)^2 &:= \frac{\int_\Omega |\mathcal{K}\phi(x) - \lambda\phi(x)|^2 d\mu(x)}{\int_\Omega |\phi(x)|^2 d\mu(x)} \\
&= \sum_{i,j=1}^{N_K} \bar{v}_i \left[\langle \mathcal{K}\psi_i, \mathcal{K}\psi_j \rangle_\mu - \lambda \langle \psi_i, \mathcal{K}\psi_j \rangle_\mu - \bar{\lambda} \langle \mathcal{K}\psi_i, \psi_j \rangle_\mu + |\lambda|^2 \langle \psi_i, \psi_j \rangle_\mu \right] v_j, \qquad (3.1)
\end{aligned}
$$

where $\bar{v}_i, \bar{\lambda}$ denote the complex conjugate of v_i, λ.

This *squared relative residual* in (3.1) is the theoretical value that measures the distance between ϕ and the eigenspace associated with λ, especially under the assumption that λ is in the discrete spectrum of $\mathcal{K}$. To approximate this residual in practice, we apply the Galerkin approximation (Boyd, 2013), which states that as the number of data points m increases, the following limits hold:

$$
\begin{aligned}
\lim_{m\to\infty} \frac{1}{m} \left[\Psi_X^* \Psi_X\right]_{ij} &= \langle \psi_i, \psi_j \rangle_\mu, \\
\lim_{m\to\infty} \frac{1}{m} \left[\Psi_X^* \Psi_Y\right]_{ij} &= \langle \psi_i, \mathcal{K}\psi_j \rangle_\mu, \qquad (3.2) \\
\lim_{m\to\infty} \frac{1}{m} \left[\Psi_Y^* \Psi_Y\right]_{ij} &= \langle \mathcal{K}\psi_i, \mathcal{K}\psi_j \rangle_\mu = \langle \psi_i, \mathcal{K}^*\mathcal{K}\psi_j \rangle_\mu,
\end{aligned}
$$

where $*$ denotes complex conjugate. Using this approximation, the *squared relative residual* from (3.1) is approximated as follows (see A.1 for more details):

$$
\widehat{\mathit{res}}(\lambda, \phi)^2 := \frac{1}{m} \mathbf{v}^* \left[\Psi_Y^* \Psi_Y - \lambda (\Psi_X^* \Psi_Y)^* - \bar{\lambda} \Psi_X^* \Psi_Y + |\lambda|^2 \Psi_X^* \Psi_X \right] \mathbf{v}. \qquad (3.3)
$$

where (3.3), denoted as $\widehat{\mathit{res}}(\lambda, \phi)^2$, represents the approximation of the theoretical value in (3.1).

By definition in (3.1), this residual quantifies the deviation from satisfying the spectral property, effectively measuring how far the estimated eigenpair deviates from the true spectrum. In practice, (3.3) can be calculated for all precomputed eigenpairs, and those with residuals below a certain threshold are retained. However, the key limitation is that while the residuals offer a way to filter and select valid eigenpairs, they do not provide a more accurate method for estimating the eigenpairs themselves.

3.2 Neural Network-ResDMD

General framework In this section, we present the Neural Network-ResDMD (NN-ResDMD) framework, designed to compute the eigenpairs of the Koopman operator directly using ResDMD-

based spectral residuals, as illustrated in Figure 1. The method first determines the optimal dictionary functions by minimizing the *total residual* $J := \sum_{i=1}^{N_K} \widehat{res}(\lambda_i, \phi_i)^2$, over all computed eigenpairs $\{(\lambda_i, \phi_i)\}_{i=1}^{N_K}$. The spectral residual directly impacts the finite-dimensional projection of the Koopman operator and our method minimizes this residual to ensure the learned basis functions adequately capture the Koopman dynamics. This approach allows the construction of the Koopman operator matrix $\tilde{K}$ without relying on external methods or post-processing. Equation (3.5) enables NN-ResDMD to compute eigenpairs directly, improving accuracy compared to ResDMD, which relies on filtering precomputed results from other methods.

In this framework, neural networks parameterize the dictionary functions $\mathbf{\Psi}(x; \theta)$, where θ represents the network parameters. This dynamic approach adapts the dictionary functions, better capturing the system's complex dynamics. By iteratively minimizing the *total residual* J, the framework produces a more accurate approximation of the Koopman operator. Unlike traditional methods like EDMD, which require manual selection of dictionary functions, the neural network-driven approach introduces greater flexibility and adaptability in representing system behavior.

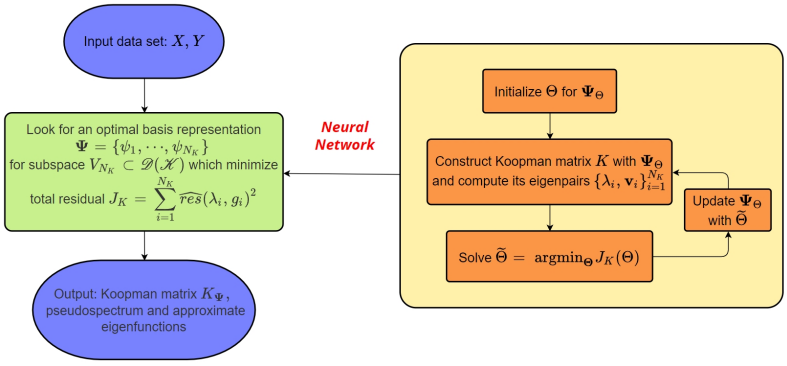

Figure 1: (Left) The classical ResDMD and (Right) the Neural Networks based ResDMD methods

From Residual to NN This section explains how neural networks are integrated into the ResDMD framework. In ResDMD, the *squared relative residual* approximation (3.3) measures how well a computed eigenpair fits the dataset. If the Koopman matrix K is well-approximated by the projected Koopman operator $\mathcal{K}_{N_K}$, the *total residual* J should approach zero as more data is provided. Thus, J can be used as a loss function, and the optimal Koopman matrix $\tilde{K}$ is obtained by minimizing:

$$J = \sum_{i=1}^{N_K} \widehat{res}(\lambda_i, \phi_i)^2. \tag{3.4}$$

which is equivalent to minimization the following (See A.2 for more details):

$$J = \frac{1}{m} \|(\Psi_Y - \Psi_X K)V\|_F^2 \tag{3.5}$$

where V is a matrix in which each column is an eigenvector $\mathbf{v}_i$ of Koopman matrix K. Thus, with a fixed dictionary function $\mathbf{\Psi}$, the explicit form for the optimal Koopman matrix $\tilde{K}$ can be directly computed as

$$\tilde{K} = G^{\dagger} A \tag{3.6}$$

where $G = \frac{1}{m}\Psi_X^* \Psi_X$, $A = \frac{1}{m}\Psi_X^* \Psi_Y$.

Remark. *Typically a regularization term is needed to enhance stability. Here we add a small perturbation, i.e.,* $\tilde{K} = (G + \sigma I)^{-1} A$ *for some small number* $\sigma > 0$.

As shown in (3.6), NN-ResDMD provides an explicit expression for $\tilde{K}$ given the *optimal* dictionary function $\mathbf{\Psi}$, allowing for the direct computation of Koopman eigenpairs. The optimization problem in Equation 3.5 is to minimize the error along the eigen-basis, in contrast to the optimization

problem $\|\Psi_Y - \Psi_X K\|_F^2$ for EDMD, thereby yielding different *optimal* $\mathbf{\Psi}$ compared to EDMD. Therefore, although the K update procedure appear identical to the EDMD approach, they originate from different theoretical foundations and serve different optimization purposes. Additionally, it automatically optimizes basis functions using neural networks, removing the need for manual selection. Since NN-ResDMD is based on the ResDMD framework, it also retains the theoretical convergence guarantees that EDMD lacks: EDMD has convergence results under strong assumptions, such as requiring the Koopman operator to be bounded (Assumption 2 in Korda & Mezić (2018)), ResDMD requires only that the operator is closed and densely defined.

In NN-ResDMD, neural networks parameterize the dictionary functions $\mathbf{\Psi}(x;\theta)$ to minimize the *total residual* $J(\theta)$, as defined in (3.4). The feedforward neural network generates the dictionary functions based on data snapshots, and the total residual is given by:

$$J(\theta) = \frac{1}{m}\|(\Psi_Y(\theta) - \Psi_X(\theta)K(\theta))V(\theta)\|_F^2 \tag{3.7}$$

where $K(\theta)$ and $V(\theta)$ depend on θ. The Koopman matrix $\tilde{K}(\theta)$ is computed as:

$$\tilde{K}(\theta) = G(\theta)^{\dagger}A(\theta) \tag{3.8}$$

with $G(\theta) = \frac{1}{m}\Psi_X(\theta)^*\Psi_X(\theta)$ and $A(\theta) = \frac{1}{m}\Psi_X(\theta)^*\Psi_Y(\theta)$.

The algorithm alternates between updating $K(\theta)$ via least squares and optimizing θ using gradient descent until $J(\theta)$ converges, yielding the approximated Koopman spectrum and optimized dictionary functions. While it is possible to optimize both $K(\theta)$ and $J(\theta)$ simultaneously, as done in Takeishi et al. (2017b) and Otto & Rowley (2019b), our separate procedure ensures computational efficiency and numerical stability compared to the coupled optimization case.

Computing Algorithm In our neural networks implementation, we include some non-trainable basis outputs to enhance the dictionary functions. Specifically, we add a vector of ones and the coordinates of the state space as non-trainable basis in the output layer, which help avoid trivial solutions, i.e., $J = 0$ for some initial θ. For the network architecture, we use the hyperbolic tangent (tanh) function as the activation function for the hidden layers. In terms of optimization, we employ the Adam optimizer for updating the network parameters. Adam is particularly well-suited for this task due to its ability to adapt the learning rate for each parameter, which can lead to faster convergence in the alternating optimization process between the network parameters and the Koopman matrix. The computing steps are illustrated in the following Algorithm 1.

Algorithm 1: NN-ResDMD

Input: Dataset X, Y, number of observables N_K, learning step δ, regularization parameter σ, loss function threshold $\epsilon > 0$.

Initialize θ, thus initializing $\mathbf{\Psi}(\theta)$ and $\tilde{K}(\theta)$;
while $J(\theta) > \epsilon$ **do**
  Update $\theta = \theta - \delta\nabla_\theta J(\theta)$;
  Compute $G(\theta) = \frac{1}{m}\Psi_X^*\Psi_X, A(\theta) = \frac{1}{m}\Psi_X^*\Psi_Y$;
  Update $\tilde{K}(\theta) = (G(\theta) + \sigma I)^{-1}A(\theta)$;
  Compute eigenvector matrix $V(\theta)$;
Solve eigenpairs $\{(\lambda_i, \phi_i = \mathbf{\Psi}\mathbf{v}_i)\}_{i=1}^{N_K}$ of $\tilde{K}(\theta)$;

Output: Eigenpairs $\{(\lambda_i, \phi_i)\}_{i=1}^{N_K}$ and $\tilde{K}(\theta)$.

If the continuous spectrum of the Koopman operator is of interest, following the ResDMD paper's idea, we can scan candidate spectrum values within a grid in the complex plane using the residuals. Specifically, we compute $\tau_j = \min_{\mathbf{v}_i \in \mathbb{C}^{N_k}} \widehat{res}(z_j, \mathbf{\Psi}(\theta)\mathbf{v}_i)$, where τ_j is the minimum residual for a grid point $z_j \in \mathbb{C}$. The approximated whole spectrum containing the continuous spectrum is then given by $\{z_j : \tau_j < \epsilon\}$.

While the practical advantages of NN-ResDMD are demonstrated through experiments, it's also worth noting that the method has theoretical underpinnings (Haykin, 2009; Weinan et al., 2019) that support its convergence properties. A brief discussion on the convergence aspects of NN-ResDMD, leveraging existing results from approximation theory in Barron spaces, is provided in Appendix

A.3. This discussion offers insights into how the neural network component of NN-ResDMD contributes to its effectiveness in approximating complex dynamical systems.

4 APPLICATION IN PHYSICAL AND BIOLOGICAL SYSTEMS

In this chapter, we present three examples that demonstrate the effectiveness of the NN-ResDMD method. In each example, we focus on estimating the three key quantities of the Koopman Mode Decomposition (KMD): eigenvalues, eigenfunctions and Koopman modes. In the first (low-dimensional) example on the classical pendulum system, we will show that our method requires significantly fewer dictionary observables compared to a similar example in (Colbrook & Townsend, 2024, Section 4.3.1, Section 6.3) when computing the spectrum of the Koopman operator and performs better in approximating continuous spectra. In the second (high-dimensional) example on turbulence, we will show that our method can detect acoustic vibrations and distinguish the pressure field by computing the Koopman modes. In the third (real-world) example on a high-dimensional neural system, we compare our method with three other popular methods in the data-driven Koopman analysis field: Hankel-DMD (Arbabi & Mezic, 2017), EDMD with Radial Basis Function (RBF) basis, and kernelized-ResDMD (Kernel ResDMD) (Colbrook & Townsend, 2024), and demonstrate the superiority of our method in identifying and clustering latent dynamic structures. These examples illustrate how our method performs in various systems, and provides a comprehensive evaluation of its capabilities.

4.1 PENDULUM

The pendulum system is a measure-preserving system due to its Hamiltonian nature, which theoretically implies that the whole spectrum should lie on the unit circle. Then we choose it as an example system with continuous spectrum. For its dynamical behaviors, if the initial position of the pendulum is sufficiently far from the peak and the initial angular speed is sufficiently small, the pendulum will oscillate; otherwise, the pendulum will pass the peak and rotate. In other words, this complex system exhibits two types of dynamical behaviors: rotation and oscillation. Here we simulate two cases with different numbers of initial points. We choose 90 and 240 initial points uniformly in the domain $[-\pi, \pi]_{per} \times [-15, 15]$. Each point evolves 1000 steps with a step size of 0.5. Thus, the total data size in each set is approximately 9×10^4 and 2.4×10^5, respectively.

As we can see in Figure 2, we only need $N_K = 300$ observables to calculate the whole spectrum approximation, which is significantly fewer than the number (nearly 1000) of observables required in (Colbrook & Townsend, 2024, Section 4.3.1) given the same data size. Moreover, even when the data size is largely increased, as seen in Figure 3, the number of necessary observables ($N_K = 350$) remains relatively small, demonstrating the robustness of efficient observables over different data sizes.

As shown in Figure 4, we compare our method to four approaches: EDMD, EDMD with Dictionary Learning (EDMD-DL), Hankel-DMD, and ResDMD, on the dataset with 90 initial points to compute the Koopman matrix and its corresponding spectral information. The first three methods (EDMD (Williams et al., 2015), EDMD-DL (Li et al., 2017), and Hankel-DMD are limited to computing eigenvalues associated with the point spectrum. In these experiments, both EDMD and ResDMD use the hyperbolic cross approximation with Hermite functions up to order 15 and Fourier functions up to order 20. Hankel-DMD uses a time delay of 150. Although Hankel-DMD yields accurate eigenvalues, it suffers from spectral pollution and requires careful tuning of the time delay parameter. With 300 basis functions, ResDMD is still unable to fully capture the whole spectrum, i.e., the unit circle, due to the insufficient number of basis functions. In the original ResDMD work, 964 basis functions using a hyperbolic cross approximation of order 100 were required to adequately cover the spectrum with a dataset of the same size (Colbrook & Townsend, 2024, Section 4.3.1). This comparison demonstrates that NN-ResDMD, even with only 300 basis functions, outperforms all four classical methods in terms of capturing the complete spectrum with greater accuracy and fewer basis functions.

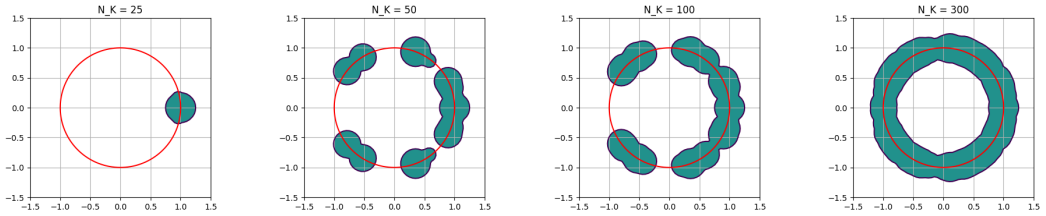

NN-ResDMD: $N_K = 25$ NN-ResDMD: $N_K = 50$ NN-ResDMD: $N_K = 100$ NN-ResDMD: $N_K = 300$

Figure 2: The four plots depict the spectrum of the Koopman operator, constructed using varying dictionary size N_K of 25, 50, 100, and 300. Each plot utilizes 90 initial points to illustrate the impact of increasing the dictionary size on approximating the spectrum of the Koopman operator.

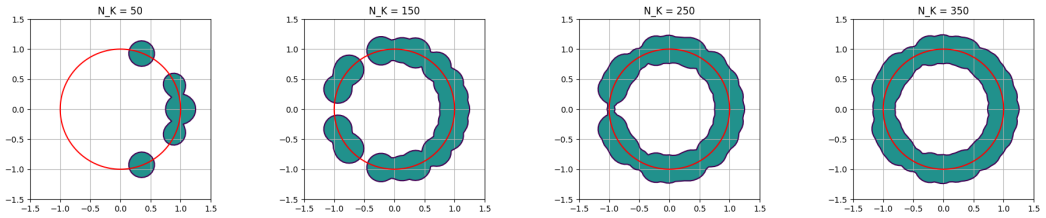

NN-ResDMD: $N_K = 50$ NN-ResDMD: $N_K = 150$ NN-ResDMD: $N_K = 250$ NN-ResDMD: $N_K = 350$

Figure 3: Same example as Figure 2 but with larger data size. Each plot utilizes 240 initial points to illustrate the impact of increasing the dictionary size on approximating the spectrum of the Koopman operator.

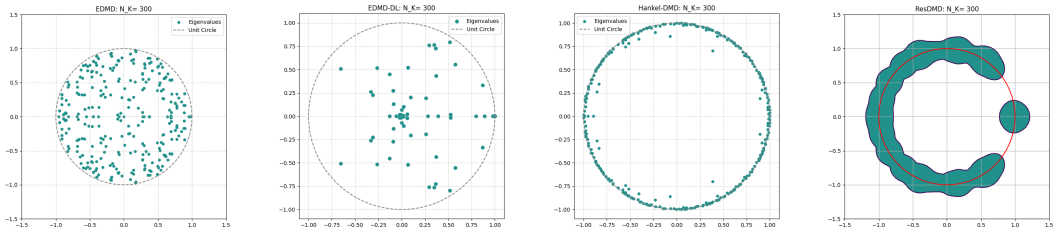

EDMD: $N_K = 300$ EDMD-DL: $N_K = 300$ Hankel-DMD: $N_K = 300$ ResDMD: $N_K = 300$

Figure 4: Comparison with classical methods. The four plots above represent the spectral information obtained from a 300×300 Koopman matrix, calculated using four different methods: EDMD, EDMD with Dictionary Learning (EDMD-DL), Hankel-DMD, and ResDMD. Each plot illustrates the eigenvalue spectrum of the Koopman operator, highlighting the differences in results produced by these methods.

4.2 TURBULENCE

Variants of DMD algorithms (Colbrook, 2023a; Tu et al., 2014; Williams et al., 2015; Rowley et al., 2009) have shown strong results in fluid dynamics. In (Colbrook & Townsend, 2024, Section 6.3), it is demonstrated that Kernel ResDMD can capture key spatial patterns and detect acoustic vibrations but requires careful selection of kernel functions.

Our method, NN-ResDMD, bypasses this by using neural networks to train observables and compute Koopman modes. Using the dataset from (Colbrook & Townsend, 2024, Section 6.3), we apply truncated Singular Value Decomposition (SVD), select 300 observables, compute Koopman modes, and project them back into the original state space.

In Figure 5, the first Koopman mode estimated by NN-ResDMD, which corresponds to the constant eigenfunction, has the smallest residual value and successfully highlights a clear global spatial separation that aligns with patterns observed in the original pressure field. The small residual values

in the figures associated with the Koopman modes confirm the estimation accuracy. This advantage allows the first Koopman mode to directly distinguish spatial features that are present in the true pressure field, which makes it a powerful tool for the interpretation of complex fluid dynamics data. Subsequent Koopman modes also reveal strong acoustic waves that are critical in various aeronautical engineering fields. In contrast, Kernel ResDMD with a generic normalized Gaussian kernel function, as shown in the original work, is unable to produce a Koopman mode similar to the first Koopman mode from NN-ResDMD that clearly distinguishes the pressure field. For comparison, we also plot four Koopman modes computed by Hankel-DMD with a time delay of 5, corresponding to the four smallest residual values, which similarly do not reveal the pressure field patterns as in NN-ResDMD. These results are presented in Appendix Figure 7.

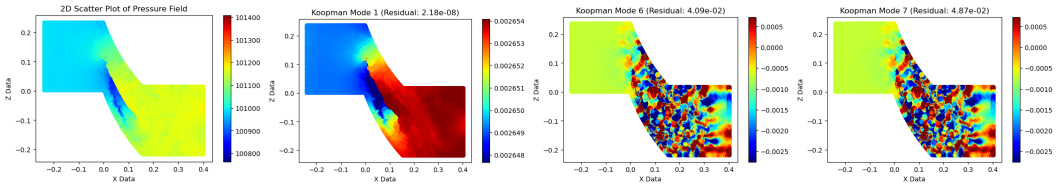

Figure 5: The plots illustrate turbulence detection with Koopman modes computed by 300 observables. The first plot shows a 2D scatter plot of the pressure field, while the other plots display various Koopman modes, each labeled with corresponding residuals.

4.3 Identification of neural dynamics in mice visual cortex

Since NN-ResDMD directly minimizes the residuals based on eigenfunctions, its estimated evolution of eigenfunctions over time should ideally capture latent dynamics. To evaluate how effectively NN-ResDMD reveals latent temporal dynamics in real data, we apply it to a dataset of high-dimensional neural signals and demonstrate its advantages over a series of classical methods: the Hankel-DMD, EDMD (combined with RBF basis) and Kernel ResDMD. These methods are selected as representative approaches for handling high-dimensional data.

The dataset is part of the open dataset on mice available for the competition 'Sensorium 2023' (Turishcheva et al., 2023; 2024). During the experiments, mice are required to look at natural videos while the neural signals are calcium imaging recordings in mice's primary visual cortex reflecting the activities of thousands of neurons. Here, we focus on a simple task of state partition of neural signals. Specifically, in each tested mouse, six video stimuli were repeatedly shown, creating ideal conditions for defining brain states. The experiment assumes that neural activity during repeated trials with the same stimuli reflects the same underlying dynamic system, allowing Koopman decomposition methods to be tested for reliably uncovering and separating these brain states.

The dataset consists of neural recordings from five mice, each exposed to 6 video stimuli, repeated 9-10 times for a total of around 60 trials. Each recording captures the activity of over 7,000 neurons, with each 10-second video sampled at 50 Hz, resulting in 300 data points per trial.

We applied NN-ResDMD and three classical Koopman decomposition methods (Hankel-DMD, EDMD with RBF basis and Kernel ResDMD) to these datasets, utilizing varying implementations and Koopman subspace dimensions. For NN-ResDMD, we trained dictionaries using all snapshots from each mouse to avoid overfitting, reducing the data to 300 dimensions via SVD and selecting 501 eigenfunctions. The decomposed eigenfunctions are shown in Figure 6A(top), with markers indicating ground truth stimulus-based state separations. For Hankel-DMD, we built a Hankel matrix with a delay of 50, producing 50 eigenfunctions per trial. In the EDMD with RBF basis approach, we employed the SVD-truncated 300 basis and 1000 RBF basis functions, resulting in 1301 eigenfunctions as temporal features. For Kernel ResDMD, we chose normalized Gaussians as kernel functions. Based on Colbrook et al. (2023), the dimension of the Koopman invariant subspace was set to the number of temporal snapshots (i.e. 299 eigenfunctions). See Appendix A.6.4 for implementation details of these methods. These eigenfunctions, plotted in Figure 6A(bottom), Appendix Figure 9A and Appendix Figure 10A, are compared against the ground truth trial identities.

The Koopman eigenfunctions represent dynamical features corresponding to the video stimuli. To evaluate their effectiveness, we assess how well eigenfunctions of the same stimuli cluster together,

distinguishing them from other states. If the eigenfunctions capture the key dynamics related to the stimuli, those from trials with the same video should be separable from others. This turns the problem into a clustering task based on the separability of eigenfunctions across different stimuli.

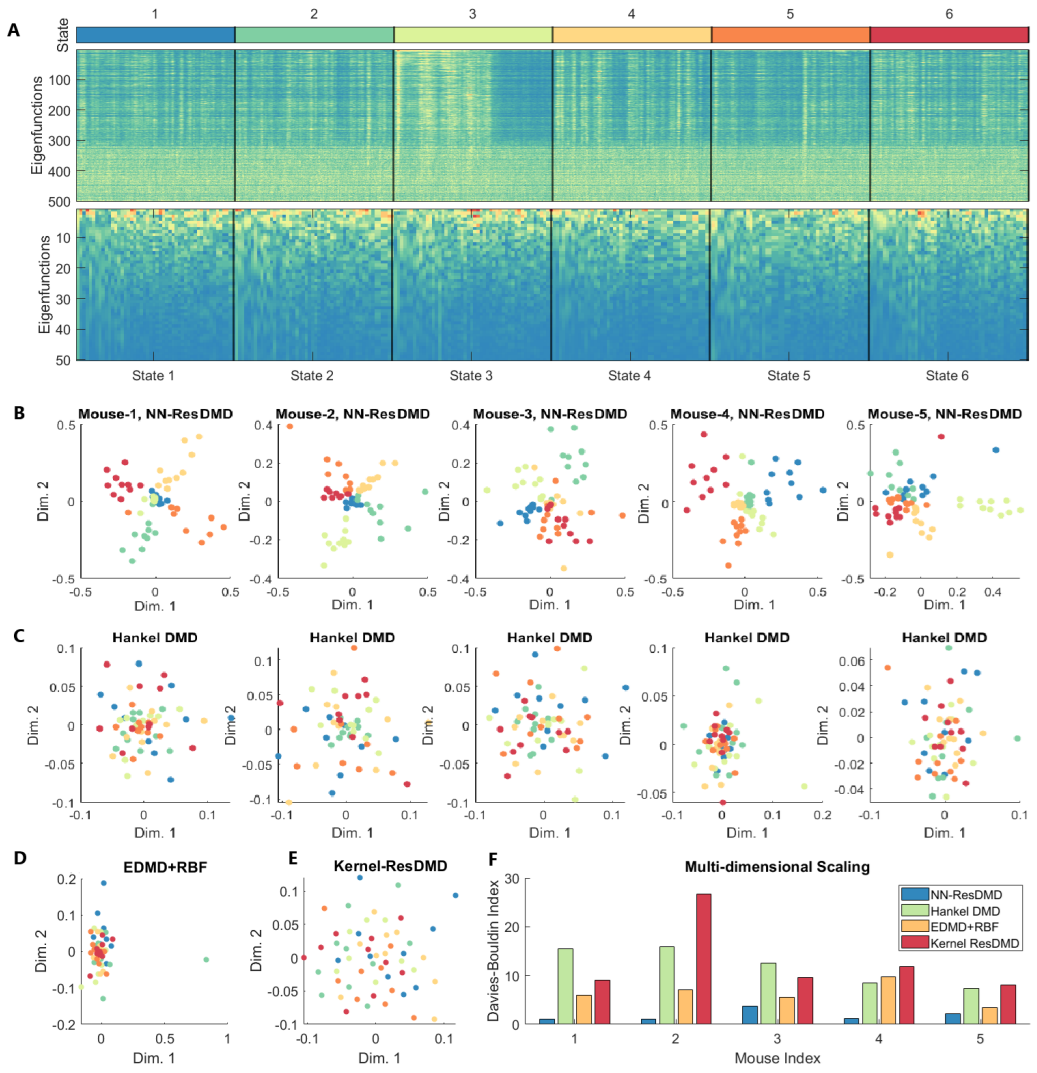

Figure 6: NN-ResDMD outperforms Hankel-DMD in identifying latent dynamic structures in neural signals with a dictionary basis of size 501. (A) (Top) 500 Koopman eigenfunctions estimated by NN-ResDMD in 6 states characterized by 6 different video stimuli in an example mouse. Eigenfunctions in each trial of each state contain 300 data points (10s with a sampling rate of 50Hz. (Bottom) 50 Koopman eigenfunctions approximated by Hankel-DMD. In line with the dimension of the Hankel matrix, each eigenfunction is 50 points long. (B) 2-D representation of Koopman eigenfunctions for each trial of all tested mice, calculated by NN-ResDMD and reduced by Multidimensional Scaling (MDS). Trials of the same state are well-clustered. (C) Same as (B) but calculated with Hankel-DMD. No clear separation of states can be seen from the reduced representation. (D) 2D representation of Koopman eigenfunctions estimated using EDMD with RBF basis for each trial in the first mouse, shown as an example. See Appendix Figure 9 for the full results. (E) Same as (D) but estimated by Kernel ResDMD for the first mouse. See Appendix Figure 10 for full results. (F) Davies-Bouldin Indices (DBIs) as a metric to evaluate the clustering quality for the two reduced representations learned by four methods (NN-ResDMD, Hankel-DMD, EDMD+RBF, and Kernel ResDMD) across five mice. Lower DBI values in the case of NN-ResDMD suggest better clustering compared to other classical methods.

We use Multi-dimensional Scaling (MDS) to visualize how these eigenfunction-based features cluster according to ground truth states. MDS reduces data dimensionality based on similarities, making it ideal for visualizing clustering performance. While UMAP and t-SNE are alternative methods, we show MDS results in 2D space (Figure 6B-E), with similar results for UMAP and t-SNE in the supplementary materials (Appendix Figure 8, Appendix Figure 9C,D and Appendix Figure 10C,D).

The 2D MDS visualization reveals clear separation of features for all 5 mice using NN-ResDMD (Figure 6B), whereas no other method shows clear clustering (Figure 6C-E, Appendix Figure 9B, Appendix Figure 10B). To quantify this clustering, we calculate the Davies-Bouldin index (DBI), a measure of clustering quality that assesses how compact and well-separated the clusters are. A lower DBI indicates more compact clusters that are farther apart from each other, which corresponds to better clustering. The DBI is significantly lower for NN-ResDMD (Figure 6F), suggesting that it captures the latent dynamic structure more effectively than all three other methods. Similar clustering patterns are confirmed with UMAP and t-SNE (Appendix Figure 11).

5 Conclusion and Future Work

Koopman spectral components (eigenpairs) are fundamental to understanding unknown dynamical systems, as they reveal the intrinsic patterns and structures underlying complex temporal behavior by providing a linear framework for analyzing nonlinear dynamics. In this paper, we introduced NN-ResDMD, a method for effectively estimating of these eigenpairs based on minimizing spectral residuals, which overcomes ResDMD's limitation by eliminating the need to filter pre-computed results. The use of neural networks to learn these eigenpairs offers a significant advantage in capturing such patterns automatically, thus enhancing adaptability and reducing the need for manual intervention in basis selection. This flexibility is particularly beneficial for high-dimensional systems where traditional approaches may struggle to uncover the underlying dynamics effectively. In this line, our experiments clearly demonstrate that NN-ResDMD significantly outperforms classical methods—including EDMD, Hankel-DMD, ResDMD and their variants—in uncovering the critical spatiotemporal characteristics of nonlinear dynamics.

Koopman eigenpairs provide unique perspectives into the interpretation of nonlinear dynamical mechanisms, and feedforward neural networks (FNNs) represent an initial step in learning spectral properties directly from data. In recent years, various deep neural network structures have been employed to learn the Koopman representations with different optimization targets other than the spectral residuals (e.g. Lusch et al. (2018); Takeishi et al. (2017b); Mardt et al. (2018); Yeung et al. (2019b); Otto & Rowley (2019b); Azencot et al. (2020a); Alford-Lago et al. (2022b); Iwata & Kawahara (2020). Therefore, future work could focus on refining neural network architectures to enhance the accuracy and efficiency of Koopman eigenpair estimation. One promising direction is the incorporation of Physics-Informed Neural Networks (PINNs) and Physics-Informed Neural Operators (PINOs), which integrate physical laws directly into the learning process. This integration will ensure that the resulting Koopman eigenfunctions align with known physical constraint, avoid overfitting and faciliatates generalization. Indeed, the integration of PINNs and PINOs with the Koopman framework has the potential to serve as a powerful bridge between data-driven and model-driven approaches, offering enhanced insights into complex systems and enabling more robust temporal evolution predictions.

References

D. J. Alford-Lago, C. W. Curtis, A. T. Ihler, and O. Issan. Deep learning enhanced dynamic mode decomposition. *Chaos: An Interdisciplinary Journal of Nonlinear Science*, 32(3):033116, 03 2022a. ISSN 1054-1500. doi: 10.1063/5.0073893. URL https://doi.org/10.1063/5.0073893.

Daniel J Alford-Lago, Christopher W Curtis, Alexander T Ihler, and Opal Issan. Deep learning enhanced dynamic mode decomposition. *Chaos: An Interdisciplinary Journal of Nonlinear Science*, 32(3), 2022b.

Hassan Arbabi and Igor Mezic. Ergodic theory, dynamic mode decomposition, and computation of spectral properties of the koopman operator. *SIAM Journal on Applied Dynamical Systems*, 16 (4):2096–2126, 2017.

Omri Azencot, N Benjamin Erichson, Vanessa Lin, and Michael Mahoney. Forecasting sequential data using consistent koopman autoencoders. In *International Conference on Machine Learning*, pp. 475–485. PMLR, 2020a.

Omri Azencot, N. Benjamin Erichson, Vanessa Lin, and Michael Mahoney. Forecasting sequential data using consistent koopman autoencoders. In Hal Daumé III and Aarti Singh (eds.), *Proceedings of the 37th International Conference on Machine Learning*, volume 119 of *Proceedings of Machine Learning Research*, pp. 475–485. PMLR, 13–18 Jul 2020b. URL https://proceedings.mlr.press/v119/azencot20a.html.

Peter J Baddoo, Benjamin Herrmann, Beverley J McKeon, J Nathan Kutz, and Steven L Brunton. Physics-informed dynamic mode decomposition (pidmd). *arXiv e-prints*, pp. arXiv–2112, 2021.

A.R. Barron. Universal approximation bounds for superpositions of a sigmoidal function. *IEEE Transactions on Information Theory*, 39(3):930–945, 1993. doi: 10.1109/18.256500.

Amit Basole, Leonard E White, and David Fitzpatrick. Mapping multiple features in the population response of visual cortex. *Nature*, 423(6943):986–990, 2003.

J.P. Boyd. *Chebyshev and Fourier Spectral Methods: Second Revised Edition*. Dover Books on Mathematics. Dover Publications, 2013. ISBN 9780486141923. URL https://books.google.ca/books?id=b4TCAgAAQBAJ.

Steven L. Brunton and J. Nathan Kutz. *Data-Driven Science and Engineering: Machine Learning, Dynamical Systems, and Control*. Cambridge University Press, 2019.

Matthew J. Colbrook. The multiverse of dynamic mode decomposition algorithms. *ArXiv*, abs/2312.00137, 2023a. URL https://api.semanticscholar.org/CorpusID:265552037.

Matthew J Colbrook. The mpedmd algorithm for data-driven computations of measure-preserving dynamical systems. *SIAM Journal on Numerical Analysis*, 61(3):1585–1608, 2023b.

Matthew J Colbrook and Alex Townsend. Rigorous data-driven computation of spectral properties of koopman operators for dynamical systems. *Communications on Pure and Applied Mathematics*, 77(1):221–283, 2024.

Matthew J Colbrook, Lorna J Ayton, and Máté Szőke. Residual dynamic mode decomposition: robust and verified koopmanism. *Journal of Fluid Mechanics*, 955:A21, 2023.

G. Cybenko. Approximation by superpositions of a sigmoidal function. *Mathematics of Control, Signals, and Systems*, 2(4):303–314, December 1989. doi: 10.1007/BF02551274. URL https://hal.science/hal-03753170.

Weinan E, Chao Ma, Stephan Wojtowytsch, and Lei Wu. Towards a mathematical understanding of neural network-based machine learning: what we know and what we don't, 2020. URL https://arxiv.org/abs/2009.10713.

David M. Grobman. Homeomorphisms of systems of differential equations. *Doklady Akademii Nauk SSSR*, 128(5):880–881, 1959.

Philip Hartman. A lemma in the theory of structural stability of differential equations. 1960. URL https://api.semanticscholar.org/CorpusID:6411725.

S.S. Haykin. *Neural Networks and Learning Machines*. Pearson International Edition. Pearson, 2009. ISBN 9780131293762. URL https://books.google.ca/books?id=KCwWOAAACAAJ.

Olivier J Hénaff, Yoon Bai, Julie A Charlton, Ian Nauhaus, Eero P Simoncelli, and Robbe LT Goris. Primary visual cortex straightens natural video trajectories. *Nature communications*, 12(1):5982, 2021.

Tomoharu Iwata and Y. Kawahara. Neural dynamic mode decomposition for end-to-end modeling of nonlinear dynamics. *ArXiv*, abs/2012.06191, 2020. URL https://api.semanticscholar.org/CorpusID:228376379.

I Kevrekidis, Clarence W Rowley, and M Williams. A kernel-based method for data-driven koopman spectral analysis. *Journal of Computational Dynamics*, 2(2):247–265, 2016.

Bernard O Koopman. Hamiltonian systems and transformation in hilbert space. *Proceedings of the National Academy of Sciences*, 17(5):315, 1931.

Bernard O. Koopman and John von Neumann. Dynamical systems of continuous spectra. *Proceedings of the National Academy of Sciences*, 18(3):255–263, 1932. doi: 10.1073/pnas.18.3.255.

Milan Korda and Igor Mezić. On convergence of extended dynamic mode decomposition to the koopman operator. *Journal of Nonlinear Science*, 28:687–710, 2018.

Joseph B Kruskal. Nonmetric multidimensional scaling: a numerical method. *Psychometrika*, 29 (2):115–129, 1964.

Yueheng Lan and Igor Mezić. Linearization in the large of nonlinear systems and koopman operator spectrum. *Physica D: Nonlinear Phenomena*, 242(1):42–53, 2013.

Qianxiao Li, Felix Dietrich, Erik M Bollt, and Ioannis G Kevrekidis. Extended dynamic mode decomposition with dictionary learning: A data-driven adaptive spectral decomposition of the koopman operator. *Chaos: An Interdisciplinary Journal of Nonlinear Science*, 27(10), 2017.

Bethany Lusch, J. Nathan Kutz, and Steven L. Brunton. Deep learning for universal linear embeddings of nonlinear dynamics. *Nature Communications*, 9, 2017. URL `https://api.semanticscholar.org/CorpusID:4854885`.

Bethany Lusch, J Nathan Kutz, and Steven L Brunton. Deep learning for universal linear embeddings of nonlinear dynamics. *Nature Communications*, 9(1):4950, 2018.

Andreas Mardt, Luca Pasquali, Hao Wu, and Frank Noé. Vampnets for deep learning of molecular kinetics. *Nature communications*, 9(1):5, 2018.

Leland McInnes, John Healy, and James Melville. Umap: Uniform manifold approximation and projection for dimension reduction. *arXiv preprint arXiv:1802.03426*, 2018.

Igor Mezić. Spectral properties of dynamical systems, model reduction and decompositions. *Nonlinear Dynamics*, 41(1-3):309–325, 2005.

Selim Onat, Peter König, and Dirk Jancke. Natural scene evoked population dynamics across cat primary visual cortex captured with voltage-sensitive dye imaging. *Cerebral cortex*, 21(11):2542–2554, 2011.

Samuel E. Otto and Clarence W. Rowley. Linearly recurrent autoencoder networks for learning dynamics. *SIAM Journal on Applied Dynamical Systems*, 18(1):558–593, 2019a. doi: 10.1137/18M1177846. URL `https://doi.org/10.1137/18M1177846`.

Samuel E Otto and Clarence W Rowley. Linearly recurrent autoencoder networks for learning dynamics. *SIAM Journal on Applied Dynamical Systems*, 18(1):558–593, 2019b.

Allan Pinkus. Approximation theory of the mlp model in neural networks. *Acta Numerica*, 8: 143–195, 1999. doi: 10.1017/S0962492900002919.

Clarence W Rowley, Igor Mezić, Shervin Bagheri, Philipp Schlatter, and Dan S Henningson. Spectral analysis of nonlinear flows. *Journal of fluid mechanics*, 641:115–127, 2009.

M. Schetzen. *The Volterra and Wiener Theories of Nonlinear Systems*. Krieger Pub., 2006. ISBN 9781575242835. URL `https://books.google.ca/books?id=hgFVAAAAYAAJ`.

Peter J Schmid. Dynamic mode decomposition of numerical and experimental data. *Journal of Fluid Mechanics*, 656:5–28, 2010.

J.J.E. Slotine and W. Li. *Applied Nonlinear Control*. Prentice Hall, 1991. ISBN 9780130408907. URL `https://books.google.ca/books?id=cwpRAAAAMAAJ`.

Naoya Takeishi, Yoshinobu Kawahara, and Takehisa Yairi. Learning koopman invariant subspaces for dynamic mode decomposition. In *Proceedings of the 31st International Conference on Neural Information Processing Systems*, NIPS'17, pp. 1130–1140, Red Hook, NY, USA, 2017a. Curran Associates Inc. ISBN 9781510860964.

Naoya Takeishi, Yoshinobu Kawahara, and Takehisa Yairi. Learning koopman invariant subspaces for dynamic mode decomposition. *Advances in neural information processing systems*, 30, 2017b.

Jonathan H. Tu, Clarence W. Rowley, Dirk M. Luchtenburg, Steven L. Brunton, and J. Nathan Kutz. On dynamic mode decomposition: Theory and applications. *Journal of Computational Dynamics*, 1(2):391–421, 2014.

Polina Turishcheva, Paul G Fahey, Laura Hansel, Rachel Froebe, Kayla Ponder, Michaela Vystrčilová, Konstantin F Willeke, Mohammad Bashiri, Eric Wang, Zhiwei Ding, et al. The dynamic sensorium competition for predicting large-scale mouse visual cortex activity from videos. *ArXiv*, 2023.

Polina Turishcheva, Paul G Fahey, Michaela Vystrčilová, Laura Hansel, Rachel Froebe, Kayla Ponder, Yongrong Qiu, Konstantin F Willeke, Mohammad Bashiri, Ruslan Baikulov, et al. Retrospective for the dynamic sensorium competition for predicting large-scale mouse primary visual cortex activity from videos. *arXiv preprint arXiv:2407.09100*, 2024.

Laurens Van der Maaten and Geoffrey Hinton. Visualizing data using t-sne. *Journal of machine learning research*, 9(11), 2008.

E Weinan, Chao Ma, and Lei Wu. Barron spaces and the compositional function spaces for neural network models. *arXiv preprint arXiv:1906.08039*, 2019.

S. Wiggins. *Introduction to Applied Nonlinear Dynamical Systems and Chaos*. Texts in Applied Mathematics. Springer New York, 2003. ISBN 9780387001777. URL `https://books.google.ca/books?id=RSI4RGdwnU4C`.

Matthew O Williams, Ioannis G Kevrekidis, and Clarence W Rowley. Data-driven approximation of the koopman operator: Extending dynamic mode decomposition. *Journal of Nonlinear Science*, 25(6):1307–1346, 2015.

Hao Wu and Frank Noé. Variational approach for learning markov processes from time series data. *Journal of Nonlinear Science*, 30(1):23–66, 2020.

Enoch Yeung, Soumya Kundu, and Nathan Hodas. Learning deep neural network representations for koopman operators of nonlinear dynamical systems. In *2019 American Control Conference (ACC)*, pp. 4832–4839, 2019a. doi: 10.23919/ACC.2019.8815339.

Enoch Yeung, Soumya Kundu, and Nathan Hodas. Learning deep neural network representations for koopman operators of nonlinear dynamical systems. In *2019 American Control Conference (ACC)*, pp. 4832–4839. IEEE, 2019b.

A APPENDIX

A.1 CALCULATION STEPS FOR 3.3

Here we are going to show how *squared relative residual* implies (3.1) and then implies (3.3). Consider $\phi = \mathbf{\Psi}\mathbf{v} = \sum_{i=1}^{N_K} \psi_i \mathbf{v}_i$ with $\|\phi\|_2 = 1$, then

$$
\begin{aligned}
&\frac{\int_\Omega |\mathcal{K}\phi(x) - \lambda\phi(x)|^2 d\mu(x)}{\int_\Omega |\phi(x)|^2 d\mu(x)} \\
&= \int_\Omega |\mathcal{K}\phi(x) - \lambda\phi(x)|^2 d\mu(x) \\
&= \langle \mathcal{K}\phi - \lambda\phi, \mathcal{K}\phi - \lambda\phi \rangle_\mu \\
&= \langle \mathcal{K}\phi, \mathcal{K}\phi \rangle_\mu - \langle \lambda\phi, \mathcal{K}\phi \rangle_\mu - \langle \mathcal{K}\phi, \lambda\phi \rangle_\mu + \langle \lambda\phi, \lambda\phi \rangle_\mu \\
&= \langle \mathcal{K}\mathbf{\Psi}\mathbf{v}, \mathcal{K}\mathbf{\Psi}\mathbf{v} \rangle_\mu - \bar{\lambda}\langle \mathbf{\Psi}\mathbf{v}, \mathcal{K}\mathbf{\Psi}\mathbf{v} \rangle_\mu - \lambda\langle \mathcal{K}\mathbf{\Psi}\mathbf{v}, \mathbf{\Psi}\mathbf{v} \rangle_\mu + |\lambda|^2 \langle \mathbf{\Psi}\mathbf{v}, \mathbf{\Psi}\mathbf{v} \rangle_\mu \\
&= \langle \sum_{i=1}^{N_K} \mathcal{K}\psi_i \mathbf{v}_i, \sum_{j=1}^{N_K} \mathcal{K}\psi_j \mathbf{v}_j \rangle_\mu - \bar{\lambda}\langle \sum_{i=1}^{N_K} \psi_i \mathbf{v}_i, \sum_{j=1}^{N_K} \mathcal{K}\psi_j \mathbf{v}_j \rangle_\mu - \lambda\langle \sum_{i=1}^{N_K} \mathcal{K}\psi_i \mathbf{v}_i, \sum_{j=1}^{N_K} \psi_j \mathbf{v}_j \rangle_\mu + |\lambda|^2 \langle \sum_{i=1}^{N_K} \psi_i \mathbf{v}_i, \sum_{j=1}^{N_K} \psi_j \mathbf{v}_j \rangle_\mu \\
&= \sum_{i,j=1}^{N_K} \bar{\mathbf{v}}_i \langle \mathcal{K}\psi_i, \mathcal{K}\psi_j \rangle_\mu \mathbf{v}_j - \bar{\lambda} \sum_{i,j=1}^{N_K} \bar{\mathbf{v}}_i \langle \psi_i, \mathcal{K}\psi_j \rangle_\mu \mathbf{v}_j - \lambda \sum_{i,j=1}^{N_K} \bar{\mathbf{v}}_i \langle \mathcal{K}\psi_i, \psi_j \rangle_\mu \mathbf{v}_j + |\lambda|^2 \sum_{i,j=1}^{N_K} \bar{\mathbf{v}}_i \langle \psi_i, \psi_j \rangle_\mu \mathbf{v}_j \\
&= \sum_{i,j=1}^{N_K} \bar{\mathbf{v}}_i \left[\langle \mathcal{K}\psi_i, \mathcal{K}\psi_j \rangle_\mu - \bar{\lambda}\langle \psi_i, \mathcal{K}\psi_j \rangle_\mu - \lambda\langle \mathcal{K}\psi_i, \psi_j \rangle_\mu + |\lambda|^2 \langle \psi_i, \psi_j \rangle_\mu \right] \mathbf{v}_j \quad (3.1) \\
&\approx \sum_{i,j=1}^{N_K} \bar{\mathbf{v}}_i \left[\frac{1}{m}[\Psi_Y^* \Psi_Y]_{ij} - \bar{\lambda}\frac{1}{m}[\Psi_X^* \Psi_Y]_{ij} - \lambda\frac{1}{m}[\Psi_Y^* \Psi_X]_{ij} + |\lambda|^2 \frac{1}{m}[\Psi_X^* \Psi_X]_{ij} \right] \mathbf{v}_j \\
&= \frac{1}{m}\mathbf{v}^* \left[\Psi_Y^* \Psi_Y - \lambda(\Psi_X^* \Psi_Y)^* - \bar{\lambda}\Psi_X^* \Psi_Y + |\lambda|^2 \Psi_X^* \Psi_X \right] \mathbf{v} \quad (3.3)
\end{aligned}
$$

Remark. *the inner product above is defined as* $\langle f, g \rangle_\mu = \int_\Omega f^* g \, d\mu(x)$

A.2 DETAILS FOR DERIVING (3.5)

$$
\begin{aligned}
J &= \sum_{i=1}^{N_K} \widehat{res}(\lambda_i, \phi_i)^2 \\
&= \sum_{i=1}^{N_K} \frac{1}{m} \mathbf{v}_i^* \left[\Psi_Y^* \Psi_Y - \lambda_i (\Psi_X^* \Psi_Y)^* - \bar{\lambda}_i \Psi_X^* \Psi_Y + |\lambda_i|^2 \Psi_X^* \Psi_X \right] \mathbf{v}_i \\
&= \sum_{i=1}^{N_K} \frac{1}{m} \left[\mathbf{v}_i^* (\Psi_Y^* \Psi_Y) \mathbf{v}_i - \mathbf{v}_i^* (\Psi_X^* \Psi_Y)^* \lambda_i \mathbf{v}_i - \mathbf{v}_i^* \bar{\lambda}_i (\Psi_X^* \Psi_Y) \mathbf{v}_i + \mathbf{v}_i^* K^* (\Psi_X^* \Psi_X) K \mathbf{v}_i \right] \\
&= \sum_{i=1}^{N_K} \frac{1}{m} \left[\mathbf{v}_i^* (\Psi_Y^* \Psi_Y) \mathbf{v}_i - \mathbf{v}_i^* (\Psi_X^* \Psi_Y)^* K \mathbf{v}_i - \mathbf{v}_i^* K^* (\Psi_X^* \Psi_Y) \mathbf{v}_i + \mathbf{v}_i^* K^* (\Psi_X^* \Psi_X) K \mathbf{v}_i \right] \\
&= \sum_{i=1}^{N_K} \frac{1}{m} \Big(\langle \Psi_Y \mathbf{v}_i, \Psi_Y \mathbf{v}_i \rangle - \langle \Psi_Y \mathbf{v}_i, \Psi_X K \mathbf{v}_i \rangle \\
&\qquad - \langle \Psi_X K \mathbf{v}_i, \Psi_Y \mathbf{v}_i \rangle + \langle \Psi_X K \mathbf{v}_i, \Psi_X K \mathbf{v}_i \rangle \Big) \\
&= \sum_{i=1}^{N_K} \frac{1}{m} \langle \Psi_Y \mathbf{v}_i - \Psi_X K \mathbf{v}_i, \Psi_Y \mathbf{v}_i - \Psi_X K \mathbf{v}_i \rangle \\
&= \sum_{i=1}^{N_K} \frac{1}{m} \| \Psi_Y \mathbf{v}_i - \Psi_X K \mathbf{v}_i \|_2^2 \\
&= \frac{1}{m} \| (\Psi_Y - \Psi_X K) V \|_F^2.
\end{aligned}
$$

Next, by matrix calculus with denominator layout convention, we try to find minimal of J:

$$
\begin{aligned}
0 = \frac{dJ}{dK} &= \frac{d \operatorname{tr}(J)}{dK} \quad \text{(since } J \text{ is a scalar)} \\
&= \frac{d}{dK} \operatorname{tr} \left(\frac{1}{m} \sum_{i=1}^{N_K} \mathbf{v}_i^* \Big[\Psi_Y^* \Psi_Y - (\Psi_X^* \Psi_Y)^* K \right. \\
&\qquad \left. - K^* (\Psi_X^* \Psi_Y) + K^* (\Psi_X^* \Psi_X) K \Big] \mathbf{v}_i \right) \\
&= \sum_{i=1}^{N_K} \frac{d}{dK} \operatorname{tr} \left(\mathbf{v}_i^* \Big[L - A^* K - K^* A + K^* G K \Big] \mathbf{v}_i \right) \\
&= \sum_{i=1}^{N_K} \frac{d}{dK} \operatorname{tr} (\mathbf{v}_i^* L \mathbf{v}_i) + \frac{d}{dK} \operatorname{tr} (\mathbf{v}_i^* A^* K \mathbf{v}_i) + \frac{d}{dK} \operatorname{tr} (\mathbf{v}_i^* K^* A \mathbf{v}_i) + \frac{d}{dK} \operatorname{tr} (\mathbf{v}_i^* K^* G K \mathbf{v}_i) \\
&= \sum_{i=1}^{N_K} -A \mathbf{v}_i \mathbf{v}_i^* - A \mathbf{v}_i \mathbf{v}_i^* + (G + G^*) K \mathbf{v}_i \mathbf{v}_i^* \\
&= \sum_{i=1}^{N_K} (-2A + 2GK) \mathbf{v}_i \mathbf{v}_i^* \quad (G \text{ is symmetric})
\end{aligned}
$$

where $\operatorname{tr}()$ is trace of a matrix and $G = \Psi_X^* \Psi_X, A = \Psi_X^* \Psi_Y, L = \Psi_Y^* \Psi_Y$.

Since eigenvector v_i is not a zero vector, $v_i v_i^*$ is not a zero matrix. So

$$-2A + 2GK = 0 \Rightarrow K = G^\dagger A.$$

Remark. *To solve* $\frac{d}{dK} \operatorname{tr} (\mathbf{v}_i^* K^* G K \mathbf{v}_i)$ *, we simply rewrite it as*

$$\frac{d}{dK} \operatorname{tr} (\mathbf{v}_i^* K^* G K \mathbf{v}_i) = \frac{d}{dK} \operatorname{tr} ((K \mathbf{v}_i)^* G (K \mathbf{v}_i))$$

A.3 Discussion On Convergence

To understand how neural networks enhance NN-ResDMD, it is important to introduce Barron space (Pinkus, 1999; Cybenko, 1989; Haykin, 2009; Barron, 1993). Barron space characterizes functions efficiently approximated by two-layer neural networks, which is central to NN-ResDMD. By leveraging networks that approximate functions within this space, NN-ResDMD can flexibly optimize the dictionary functions for Koopman operator approximation, making it highly effective for complex, high-dimensional systems.

A function f belongs to Barron space $\mathcal{B}$ if it can be represented as:

$$f(x) = \int_{\Omega} a\sigma(w^T x)\rho(da, dw),$$

where σ is the activation function, w is a weight vector, a is a coefficient, and ρ is a probability distribution. The complexity of f is measured by the Barron norm $\|f\|_{\mathcal{B}}$:

$$\|f\|_{\mathcal{B}} = \inf_{\rho \in P_f} \left(\int_{\Omega} |a| \|w\|_1 \rho(da, dw) \right),$$

where P_f is the set of distributions for which f can be represented. This framework provides a basis for analyzing approximation errors in neural networks.

The following theorem (E et al., 2020) discusses the approximation capabilities of two-layer neural networks within this context, establishing a foundation for the subsequent analysis.

Theorem A.1 (Direct Approximation Theorem, L^2-version)**.** *For any $f \in \mathcal{B}$ and $r \in \mathbb{N}$, there exists a two-layer neural network f_r with r neurons $\{(a_i, \mathbf{w}_i)\}$ such that*

$$\|f - f_r\|_{L^2} \lesssim \frac{\|f\|_{\mathcal{B}}}{\sqrt{r}}.$$

This result implies that the approximation error decreases at a rate of $1/\sqrt{r}$ as the number of neurons r increases, with the constant $\|f\|_{\mathcal{B}}$ reflecting the complexity of the function f within the Barron space.

Now, consider a Barron space $\mathcal{B}$ which is dense in $L^2(\Omega, \mu)$ and a projected Koopman operator $\mathcal{K}_{N_K} : \mathcal{B}_{N_K} \to L^2(\Omega, \mu)$ where $\mathcal{B}_{N_K} \subseteq \mathcal{B}$ is a N_K-dimensional subspace spanned by some dictionary $\mathbf{\Psi} = \{\psi_i\}_{i=1}^{N_K}$. According to Theorem A.1, we can have a well-trained dictionary that almost spans $\mathcal{B}_{N_K}$, i.e., given $\epsilon > 0$, we can always obtain a dictionary $\mathbf{\Psi}_r = \{\psi_{r,i}\}_{i=1}^{N_K}$ such that $\sum_{i=1}^{N_K} \|\psi_{r,i} - \psi_i\|_2^2 < \epsilon$.

A.4 Source code

For reproducibility, the source code will be available at the following anonymous URL: https://anonymous.4open.science/r/ICLR-7305-PROJ. A full version of the codebase will be released upon acceptance of the paper.

A.5 Koopman Modes Computed by Hankel-DMD

Here we present the Koopman modes computed by Hankel-DMD for comparison with the NN-ResDMD results. As shown in Figure 7, despite having small residuals, these modes fail to clearly capture the fundamental pressure field structure that was successfully identified by NN-ResDMD's first Koopman mode (see Figure 5). This comparison demonstrates the superior ability of NN-ResDMD to extract physically meaningful patterns from complex fluid systems.

A.6 Practical details for neural data analysis

A.6.1 Dataset Details and Experimental Setup

The dataset utilized in this study is part of the open dataset provided for the 'Sensorium 2023' competition (Turishcheva et al., 2023). The dataset consists of calcium imaging recordings from the

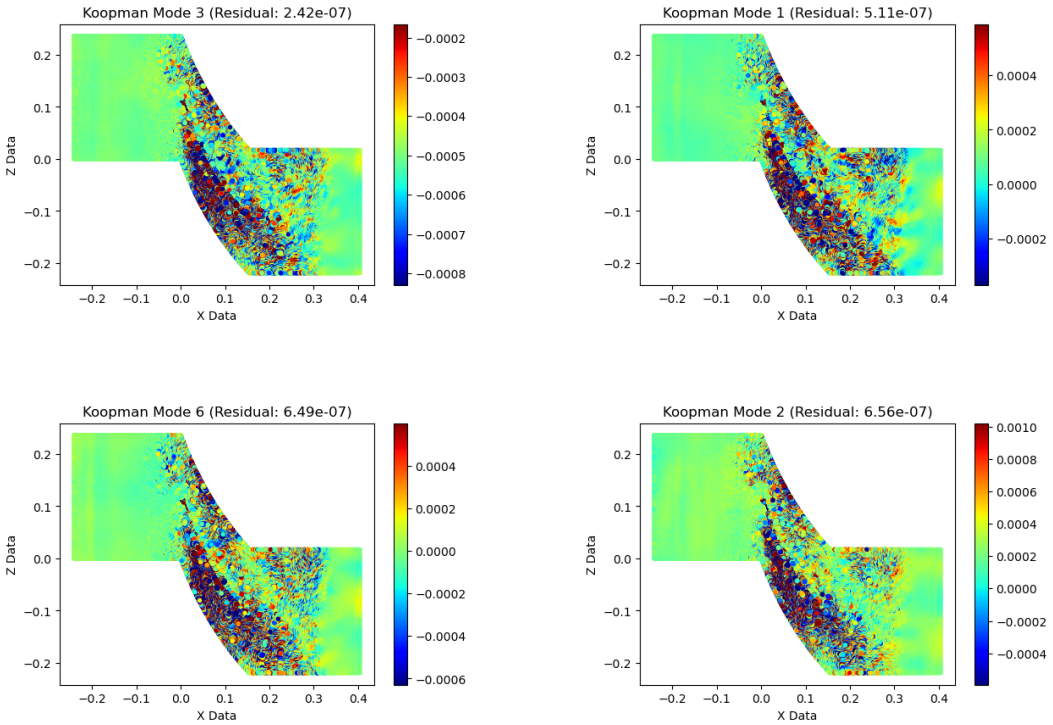

Figure 7: The plots illustrate turbulence detection using the four Koopman modes computed by Hankel-DMD, which are ranked with their corresponding residuals from the smallest.

primary visual cortex of mice. During the experiments, the mice were presented with natural video stimuli while the activity of thousands of neurons was recorded. The objective of the competition is to predict large-scale neuronal population activity in response to different frames of the stimulus videos, based on the hypothesis that population dynamics in the primary visual cortex, driven by visual stimuli, encode significant information about the dynamics of the videos (Basole et al., 2003; Onat et al., 2011; Hénaff et al., 2021).

A.6.2 Task Definition and Rationale

In contrast to the competition's prediction objective, our study focuses on the task of state partitioning of neural signals. While prediction remains feasible, we aim to demonstrate that state partitioning is sufficient to highlight the superiority of NN-ResDMD over a series of other methods in uncovering the latent dynamics of the system. Specifically, in each experiment, a set of six video stimuli was repeatedly presented to each mouse, creating ideal conditions for defining brain states. The recording setup remained consistent for each mouse, ensuring that the neural activities could be interpreted as originating from the same dynamical system, with the primary variable being the input stimulus.

We hypothesize that during repeated trials with identical visual stimuli, the underlying dynamics of the neural system remain consistent. Consequently, the recurrence of the same brain state is expected during these trials. This provides a reliable basis for testing the efficacy of Koopman decomposition methods in uncovering latent dynamics and distinguishing these states.

A.6.3 Dataset Structure and Dimensionality

The dataset includes neural recordings from five mice, with each mouse responding to six distinct video stimuli, presented in 9-10 repeated trials (resulting in approximately 60 trials in total). Each trial involves recordings of over 7000 neurons. The duration of each video stimulus is 10 seconds,

with a sampling rate of 50 Hz, yielding 300 data points (299 snapshots) per trial. Thus, the data to be analyzed consists of a high-dimensional time series with 7000+ observables per snapshot.

A.6.4 IMPLEMENTATIONS OF NN-RESDMD AND OTHER CLASSICAL METHODS

We compare here four methods: the proposed NN-ResDMD and three classical Koopman decomposition methods for high-dimensional systems: the Hankel-DMD, the EDMD with RBF basis, and the Kernel ResDMD. We applied them to the 5 datasets, although with slightly different implementations and different dimensions of approximated Koopman invariance subspace.

For NN-ResDMD, we train the dictionaries with all the snapshots recorded in each mouse such that the total snapshot number is the product of the snapshot number in one trial and the number of all trials. This is to avoid overfitting with the small snapshot numbers within a trial. The high-dimensional data is first reduced to 300 dimensions with Singular Value Decomposition. The dimension of the Koopman subspace is chosen to be 601, consisting of 300 trained bases and 301 pre-chosen ones (constant and the first-degree polynomials of the SVD-ed 300 dimensions). The first 501 eigenfunctions sorted by the modulus of eigenvalues are selected to avoid spurious eigenvalues estimation due to noise. One can find the decomposed eigenfunctions in Figure 6A(top), with a marker of the ground truth state separations based on stimulus identity.

For Hankel-DMD, the Koopman eigenfunctions were approximated using the eigenvectors of the Hankel matrix. Specifically, the Hankel matrix was formed as in Equation 53 from Arbabi & Mezic (2017), using all the observables from one trial of each mouse with a delay of 50. Consequently, the snapshot size became 249 times the observable number, and the resulting number of eigenfunctions was 50, each with a length of 50. The Hankel-DMD eigenfunctions for each trial of data are shown in Figure 6A (bottom), alongside the ground truth trial identities for comparison.

For EDMD with RBF basis, the high-dimensional dataset is first reduced to 300 dimensions with SVD. Then RBF basis is calculated with 1000 RBF functions. The choice of the basis number is decided based on classical experiments of using RBF basis to estimate the Koopman operator of Duffing systems (Li et al., 2017).

For Kernel ResDMD, as it is a variant of Kernel EDMD (Kevrekidis et al., 2016), the dimension of the Koopman invariant subspace should corresponds to the sample number (in time). Given the data size to be 300, we have 299 snapshots, resulting in 299 Koopman bases. The detailed calculated is performed for each trial with the program provided in the original ResDMD paper (Colbrook et al., 2023; Colbrook & Townsend, 2024). We chose the kernel function as the commonly-used normalized Gaussian function in the calculation.

The Koopman eigenfunctions from both NN-ResDMD and other methods represent dynamical features corresponding to one of the six video stimuli. To evaluate how well the eigenfunctions capture the latent dynamics, we assess the similarity of the features for trials with the same stimulus and their dissimilarity from those corresponding to different stimuli. Effectively, this makes the problem a clustering task, where the separability of the Koopman eigenfunctions reflects how well they capture the key dynamic components related to the stimuli.

A.6.5 VISUALIZATION AND CLUSTERING PERFORMANCE

To visualize the clustering of high-dimensional Koopman eigenfunctions, we perform dimensionality reduction using Multi-dimensional Scaling (MDS). MDS is particularly useful for visualizing high-dimensional data by preserving pairwise similarities (Kruskal, 1964) (here we use correlation as a measure of similarities). While UMAP (McInnes et al., 2018) and t-SNE (Van der Maaten & Hinton, 2008) are alternative visualization methods, with different emphasis on global-local relationships, we primarily use MDS in this study and provide UMAP and t-SNE results in the supplementary materials (see Appendix Figure 8A, B, Appendix Figure 9C, D and Appendix Figure 10C, D). UMAP in implementation is still correlation-based. For t-SNE estimation we use the perplexity of 15, as a value for optimal separation.

By applying MDS, the high-dimensional eigenfunction-based features are reduced to a low-dimensional space. For illustration, we present the results of reducing the feature space to two dimensions (Figure 6B-E). The NN-ResDMD reduced features for the six types of trials (corresponding to the six video stimuli) are well-separated for all five mice (Figure 6B). In contrast, the

Hankel-DMD features show no clear clustering structure (Figure 6C). Similarly, the features produced by EDMD with an RBF basis and Kernel ResDMD do not show clear separability (Figure 6D-E, Appendix Figure 9B-D, Appendix Figure 10B-D).

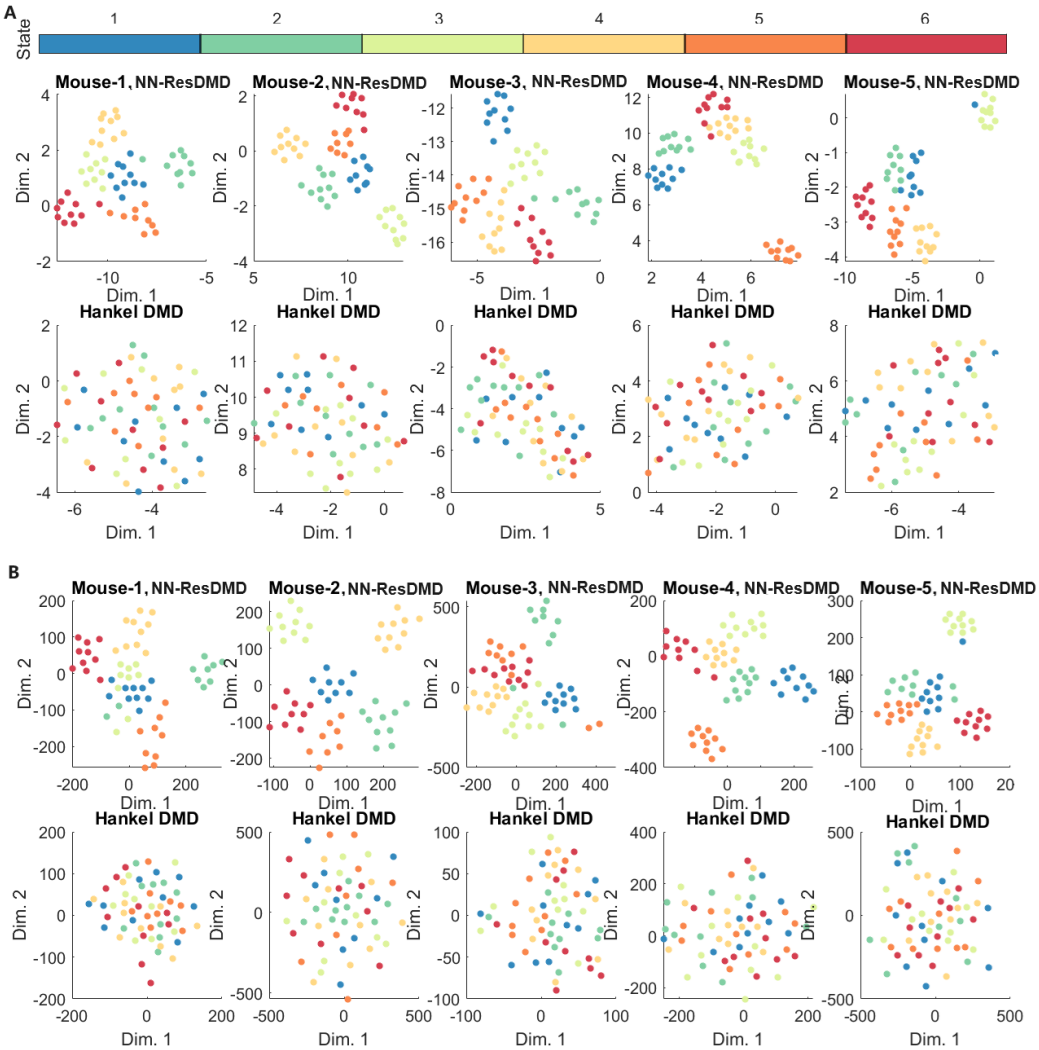

Figure 8: State Partition performance of eigenfunctions for NN-ResDMD and Hankel-DMD in 2D space visualized with UMAP (A) and t-SNE (B).

A.6.6 Clustering Quality Metrics

We further quantified the clustering quality by calculating the Davies-Bouldin Index (DBI) for both Koopman decomposition methods across all mice (Figure 6F). The DBI is designed to assess the compactness of clusters and the separability between them. A lower DBI indicates better clustering performance. NN-ResDMD features yield significantly lower DBI scores compared to other methods, confirming that NN-ResDMD produces more clearly defined clusters corresponding to the ground truth trials. Similar clustering results are observed with UMAP and t-SNE (see Appendix Figure 11), further supporting the superior performance of NN-ResDMD in capturing the latent dynamic structure compared to the other classical methods.

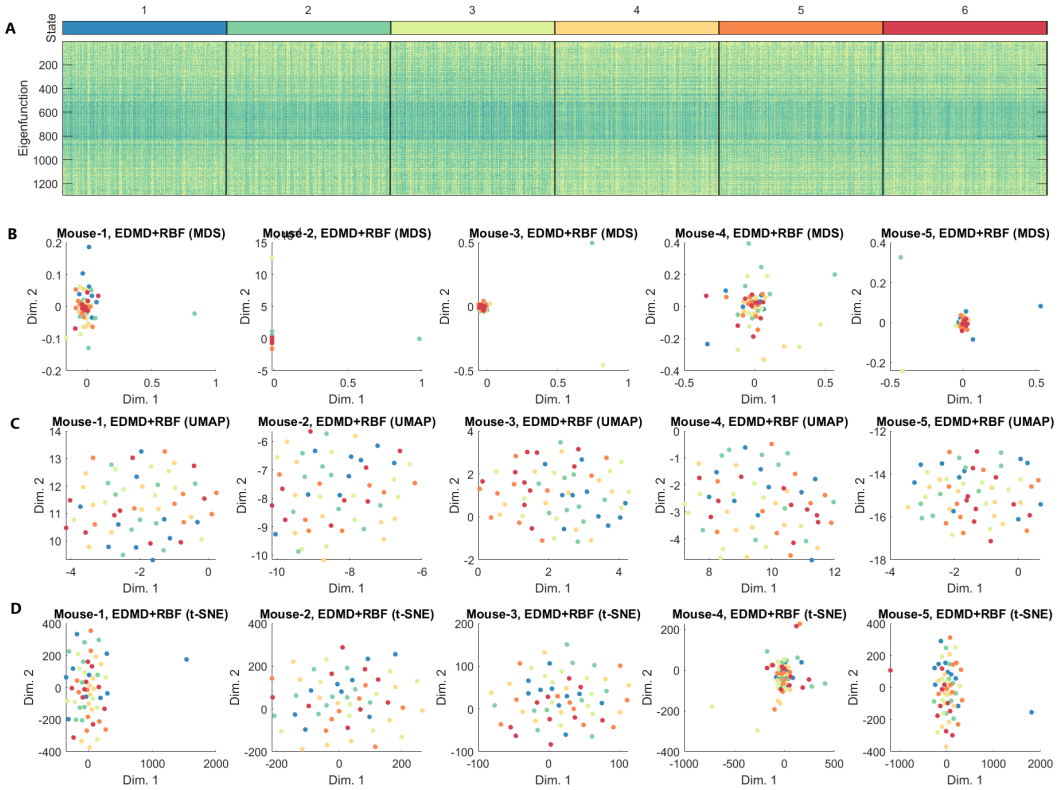

Figure 9: Full results of EDMD with RBF basis. (A) 1301 Koopman eigenfunctions estimated by EDMD with RBF basis in 6 states characterized by 6 different video stimuli in an example mouse. Eigenfunctions in each trial of each state contain 300 data points (10s with a sampling rate of 50Hz). (B) 2-D representation of Koopman eigenfunctions for each trial of all tested mice, calculated by EDMD with RBF basis and reduced by Multidimensional Scaling (MDS). No clear separation of states can be seen from the reduced representation. (C) Same as (B) but visualized with UMAP. No clear separation of states can be seen from the reduced representation. (D) Same as (C) but visualized with t-SNE. No clear separation of states can be seen from the reduced representation.

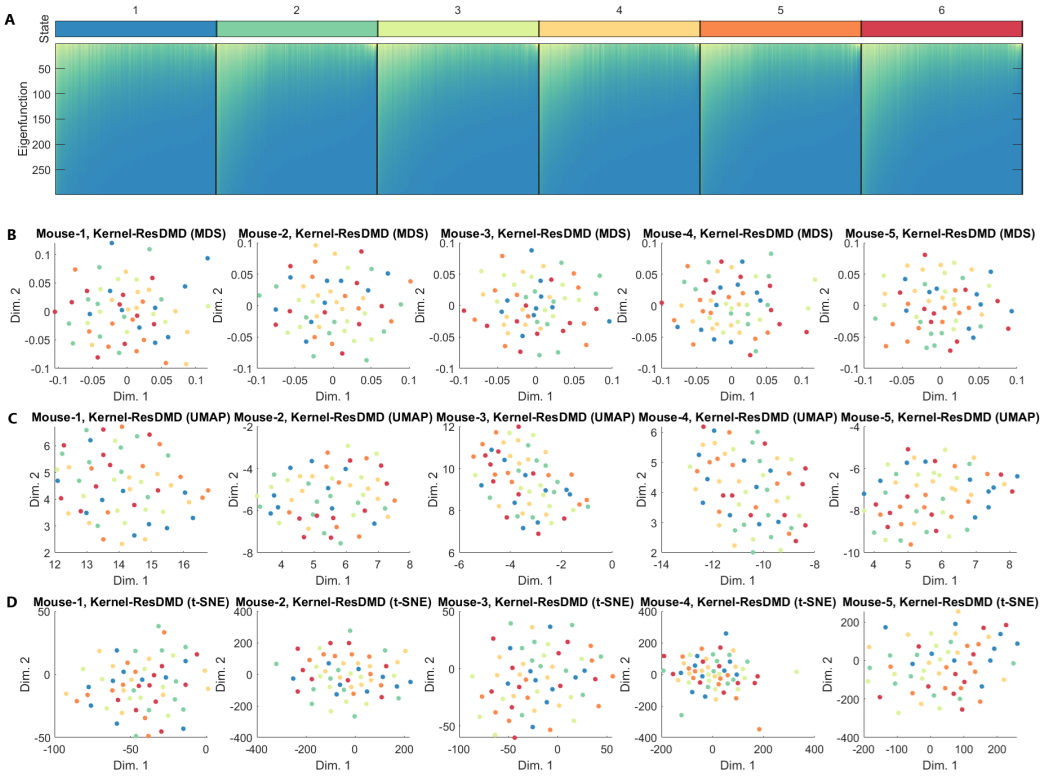

Figure 10: Same as Figure 9 but estimated with Kernel ResDMD, with 299 basis of the Koopman subspace, thus 299 eigenfunctions.

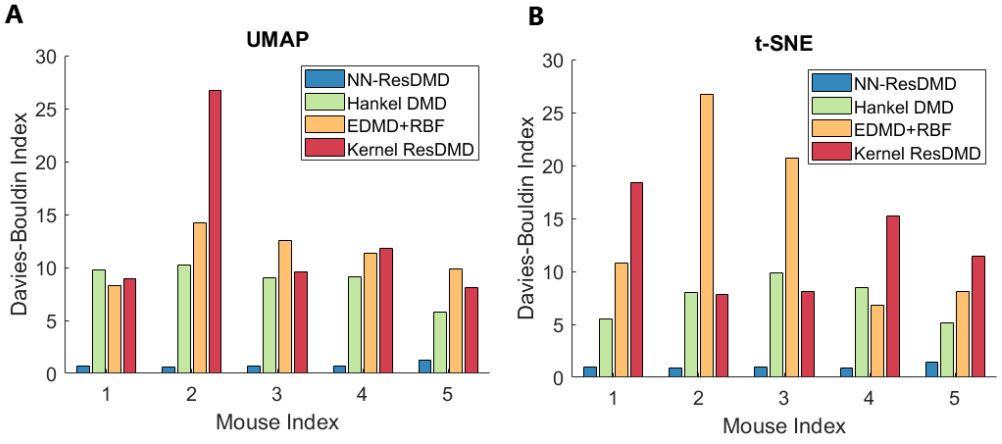

Figure 11: Davies-Bouldin Indices evaluating the clustering performance of dynamical components learned by four methods (NN-ResDMD, Hankel DMD, EDMD+RBF, and Kernel ResDMD) across five mice. Comparisons are shown using UMAP (A) and t-SNE (B).